Site-specific quasi in situ investigation of primary static recrystallization in a low carbon steel

Diehl, Martin; Kertsch, Lukas; Traka, Konstantina; Helm, Dirk; Raabe, Dierk

DOI
10.1016/j.msea.2019.02.032

Publication date
2019

Document Version
Accepted author manuscript

Published in
Materials Science and Engineering A

Citation (APA)
Diehl, M., Kertsch, L., Traka, K., Helm, D., & Raabe, D. (2019). Site-specific quasi in situ investigation of primary static recrystallization in a low carbon steel. *Materials Science and Engineering A*, *755*, 295-306. https://doi.org/10.1016/j.msea.2019.02.032

Materials Science & Engineering A xxx (xxxx) xxx-xxx

Contents lists available at ScienceDirect

Materials Science & Enginering A

journal homepage: www.elsevier.com

Site-specific quasi *in situ* investigation of primary static recrystallization in a low carbon steel

Martin Diehl [a], [*], Lukas Kertsch [b], Konstantina Traka [a], [c], Dirk Helm [b], Dierk Raabe [a]

[a] *Max-Planck-Institut für Eisenforschung GmbH, Max-Planck-Straße 1, 40237 Düsseldorf, Germany*
[b] *Fraunhofer-Institut für Werkstoffmechanik IWM, Wöhlerstraße 11, 79108 Freiburg, Germany*
[c] *Department of Materials Science and Engineering, TU Delft, Mekelweg 2, 2628 CD Delft, the Netherlands*

ARTICLE INFO

Keywords:
Recrystallization
DC04 steel
EBSD
Site-specific characterization
In situ

ABSTRACT

Low-alloyed steels with body-centered cubic crystal structure are a material class that is widely used for sheet metal forming applications. When having an adequate crystallographic texture and grain morphology, their mechanical behavior is characterized by an isotropic in-plane flow behavior in combination with a low yield strength. The decisive processing steps for obtaining these beneficial mechanical properties are cold rolling and subsequent annealing. While for the former the number of passes, the deformation rates, and the total thickness reduction are the main processing parameters, the latter is described mainly by the heating rate and the holding temperature and time. Primary static recrystallization during annealing subsequent to the cold rolling process alters mainly two aspects of the material state: It firstly replaces the elongated and heavily deformed grains of the cold rolled microstructure by small, globular grains with low dislocation density and secondly it changes the crystallographic texture insofar as it typically diminishes the α- and strengthens the γ-fiber texture components. In the present work, the recrystallization behavior of a commercial non-alloyed low carbon steel is studied. A quasi *in situ* setup that enables site-specific characterization is employed to gain a local picture of the nucleation and recrystallization process. From the Kernel Average Misorientation (KAM) values of the deformation structure, the tendency to be consumed by new grains can be predicted. Crystallographic analysis shows that the most deformed regions have either a γ-fiber orientation or belong to heavily fragmented shear band regions. New grains nucleate especially in such highly deformed regions and inherit often the orientation from the deformation microstructure.

1. Introduction

Low-alloyed steels with body-centered cubic crystal structure (bcc, ferrite) are a material class that is widely used in automotive sheet metal forming applications. When having an adequate crystallographic texture and grain morphology, their mechanical behavior is characterized by an isotropic in-plane flow behavior—i.e. a high r value and a low Δr value[1]—in combination with a low yield strength [13]. The decisive industrial processing steps for obtaining these beneficial mechanical properties are cold rolling and subsequent annealing. While for the former the number of passes, the deformation rates, and the total thickness reduction are the main processing parameters, the latter is described mainly by the heating rate and the holding temperature and time.

As a topic of high industrial relevance, the evolution of microstructure and crystallographic texture resulting from primary static recrystallization [7] during the annealing step has been extensively studied, e.g. by Hölscher et al. [13], Raabe and Lücke [32,33], Inagaki [20], Hutchinson [19], Samajdar et al. [36,37], Barnett [3], and Barnett Kestens [5]. From these previous studies[2] it is known that a comprehensive understanding of recrystallization requires to consider the full thermo–chemo–mechanical history of the material, starting at least with its state after hot rolling.

Some features already present in the hot rolled state remain mostly unchanged during cold rolling and can, therefore, influence the recrystallization behavior. These features include chemical inhomogeneity and—with the exception of changes due to internal fracture—precipi-

---

[*] Corresponding author.
Email address: m.diehl@mpie.de (M. Diehl)

https://doi.org/10.1016/j.msea.2019.02.032
Received 9 January 2019; Accepted 9 February 2019
Available online xxx
0921-5093/ © 2019.

tate size and distribution. Moreover, despite the severe texture formation during cold rolling, even certain recovery texture components from the hot rolling texture can be passed down to the deformation texture [32,31,2].

During cold rolling the grains accumulate high defect densities, i.e. mainly dislocations, and form crystallographic textures which are characteristic for the imposed near-plane strain deformation. In most low carbon steels the cold rolling texture is characterized by the gradual build up of a pronounced α-fiber (<1 1 0>‖ Rolling Direction, RD) and γ-fiber (<1 1 1>‖ Normal Direction, ND) texture [17]. Typically, the α-fiber texture accumulates lower dislocation densities and weaker local orientation gradients compared to most texture components on the γ-fiber.[3]

Primary static recrystallization during annealing subsequent to the cold rolling process alters mainly two aspects of the material state: It firstly replaces the elongated and heavily deformed grains of the cold rolled microstructure by small, globular grains with low dislocation density and secondly it changes the crystallographic texture insofar as it often diminishes the prevalent α- and strengthens the γ-fiber texture components [36,37]. The recrystallization tendency correlates strongly with the crystallographic orientation as the latter determines the degree of plastic deformation and, hence, the stored energy. Recovery in regions with low recrystallization tendency can further amplify the differences in stored energy, even to such an extent that only partial recrystallization occurs. Other factors retarding or hampering recrystallization include grain boundary pinning due to second phase particles [10,25], impurity drag due to solute decoration of the grain boundaries and the limited mobility of grain boundary junctions [11].

For beneficial mechanical properties, i.e. good formability, a fully recrystallized microstructure that consists of small globular grains and a pronounced γ-fiber is desirable [27]. Such a microstructure can only be obtained when sufficient preceding deformation provides a high enough driving force for recrystallization, the heating rate is fast enough to suppress extensive recovery, and the annealing lasts for a sufficient amount of time to allow for newly formed crystals to sweep the adjacent deformation microstructure. For low carbon steels, a thickness reduction by at least 60% during cold rolling, heating rates higher than several Ks^{-1}, and a annealing time of 1 min or longer at temperatures above 600 °C should result in a fully recrystallized microstructure [4].

In the present work, the recrystallization behavior of a commercial non-alloyed low carbon steel (DC04 grade) is studied. A quasi *in situ* setup [23,26,41,40] that enables site-specific characterization is employed to gain a local picture of the nucleation and recrystallization process. This approach, which is based on scanning electron microscopy/electron backscatter diffraction imaging (SEM/EBSD) allows to link nucleation and growth directly to microstructural features such as grain shape, crystallographic orientation, and deformation level. For an investigation on the effects of second phase particles the material is characterized additionally by secondary electron (SE) imaging. More specifically, the influence of Fe_3C carbides at the grain boundaries and dispersed manganese sulphide (MnS) precipitates is investigated. Finally, the combination of multiple measurement series allows to complement the observed behavior at the microstructure scale with global texture evolution data.

The study is structured as follows: First, in Section 2, the material is specified and the two employed experimental setups are presented. The results are presented in Section 3 which form the basis for the following discussion (Section 4).

2. Experimental investigation

2.1. Material

The material used in this study is a DC04 mild steel. Its chemical composition, measured with infrared absorption after combustion (content of C and S) and Inductively Coupled Plasma and Optical Emission Spectrometry (ICP-EOS, remaining elements), is given in Table 1. It can be seen that the carbon content is only slightly above half of the maximum of 0.08 wt% permissible for the investigated grade.

The material was industrially cold rolled to approximately 65% thickness reduction. Fig. 1 shows optical micrographs of the hot rolled and subsequently cold rolled material. The hot rolled microstructure (Fig. 1a) consists of globular grains and two different kinds of precipitates: small globular MnS precipitates are randomly distributed within the grains and larger carbides (Fe_3C) are located along the grain boundaries. As a consequence of cold rolling, the initially globular grains became elongated and some of the carbides broke up into smaller pieces (Fig. 1b).

2.2. Quasi in situ recrystallization observation approach

The employed quasi *in situ* characterization approach, presented in similar form e.g. by Zhang et al. [41] and Zeng et al. [40], is based on interrupted annealing heat treatments. Interrupting the heat treatment is necessary to perform site-specific EBSD imaging which has an acquisition time much longer than the time required for full recrystallization in the investigated material in cold rolled state. Two challenges are associated with this approach: Firstly, a high quality of the sample surface for the EBSD measurements needs to be preserved, i.e. deterioration due to oxidation needs to be avoided. Secondly, recovery processes during heating up and cooling down for the measurements should be minimized. It should be noted that, while several studies reveal that the free surface only has a minor influence on the recrystallization behavior [15,14,16], nucleation events in the subsurface material cannot be tracked with this approach.

In the following, the two setups used in this study to perform the measurements are presented. In both setups, a polished sample (surface ‖ ND) was first characterized by means of EBSD and SE and then heat treated and characterized with EBSD several times.

2.2.1. Setup A

The first setup consists of a Gleeble 3150 integrated digital closed loop control thermal and mechanical testing system and a Zeiss SUPRA 40VP scanning electron microscope with TSL Orientation Imaging Microscopy for EBSD.

In order to minimize oxidation, the evacuated test chamber was twice flushed with Argon before the experiment. Then, the heat treatment was performed in a low-pressure Argon atmosphere. At the beginning of each cycle, the sample was heated up by resistance heating to 600 °C within 5 s using a two step procedure in order to prevent an overshoot of the temperature. To rapidly cool down the sample for the EBSD characterization, the heat discharge of the cooled jaws was enhanced by exposing the sample to an Argon stream. By this, a cooling rate of $-40\,\mathrm{Ks}^{-1}$ until 300 °C was reached. The measured time–temperature diagram of one experiment is shown in Fig. 2a. Since after several heat treatment cycles the quality of the polished surface was not sufficient for EBSD characterization any more, for total annealing times longer than 20 s the sample was slightly re-polished after the heat treatment steps. Scans were taken with a step width of 0.5 µm. After the last heat treatment step, the specimen was etched with 3% nitric

---

[1] r and Δr denote the Lankford coefficient and the planar anisotropy, respectively [6].

[2] see also the older overview articles by Hutchinson [18] and Ray et al. [34] and the concise, recent one by Kestens Pirgazi [22].

[3] Note that an orientation can belong at the same time to the α-fiber and the γ-fiber.

Table 1
Chemical composition of the investigate material in wt%. Balance is Fe.

C	Mn	Cr	Cu	Mo	N	Ni	P	S	Si	Al	Ti
0.044	0.185	0.0186	0.0225	0.0017	0.0052	0.0105	0.0066	0.0121	0.0060	0.0426	0.0013

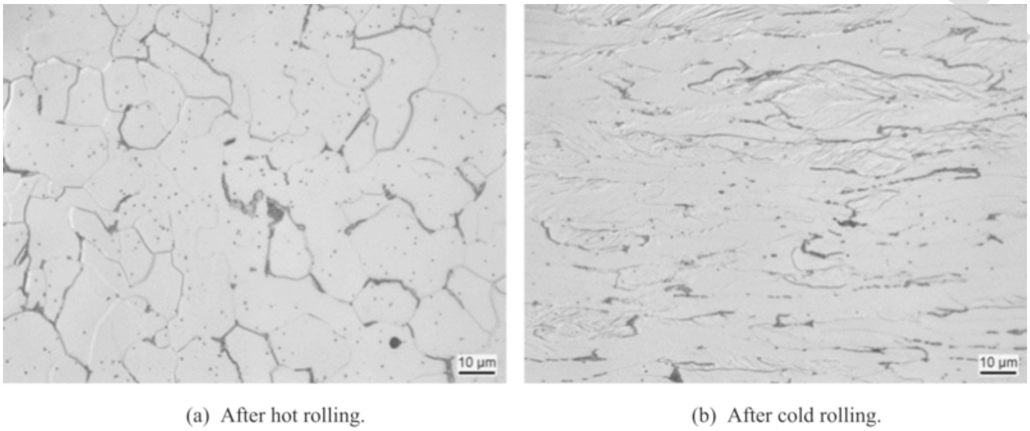

(a) After hot rolling.
(b) After cold rolling.

Fig. 1. Light microscopy images of the DC04 microstructure. The material in cold rolled condition was used in this study. The view is parallel to ND, RD is horizontal.

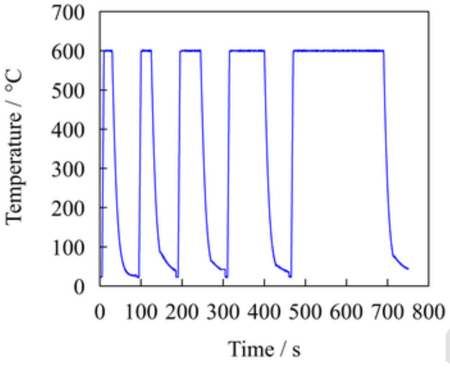

(a) Setup A, sample 1.

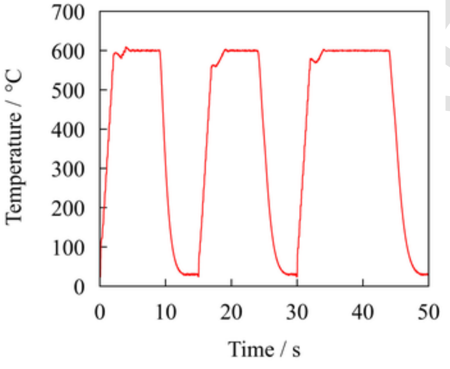

(b) Setup B, sample 5.

Fig. 2. Measured temperature-time profile.

acid in ethanol and investigated by SE and energy-dispersive X-ray spectroscopy (EDX).

2.2.2. *Setup B*

For the heat treatment in this setup, a Bähr DIL 805A/D dilatometer was employed. To prevent corrosion, the chamber of the dilatometer was evacuated and flushed with Argon three times before each heating cycle. The experiment itself was conducted in a low-pressure Argon atmosphere. Via inductive heating the sample was heated up from room temperature to 600 °C in 4 s (average heating rate of 145 $\mathrm{Ks^{-1}}$). Flushing with Nitrogen enabled cooling rates of approx. $-150\,\mathrm{Ks^{-1}}$ until 100 °C was reached, see Fig. 2b). As in setup A, the overshooting of the temperature owing to the limited response time of the control system at high heating rates was minimized by decreasing the heating rate before approaching the target temperature. However, despite decreasing the heating rate at 530 °C, overshooting could not be completely prevented (see Fig. 3). A JEOL JSM 6500F FEG-SEM microscope with an EDAX/TSL detector was used for EBSD and SE characterization. EBSD measurements have been performed at a step width of 0.25 μm, a small safety margin ensured that an overlapping area for each sample was characterized.

2.3. *Post processing*

The orientation data has been processed and analyzed with the TSL OIM software in version 5.3 and 7.3, respectively. Filtering operations include Neighbor Orientation Correlation, Neighbor CI (Confidence Index) Correlation, Grain CI Standardization, and Dilation. Additional analysis, such as calculating the orientation distribution functions (ODF) to plot pole figures, has been performed with the MTEX toolbox for MATLAB [1].

3. Results

Altogether, results of six specimens are presented. Two specimens have been heat treated using setup A for a total nominal time of 400 s (sample 1, five steps) and 360 s (sample 2, six steps), respectively. After cropping all scans to the same area, they have a size of 146 μm × 170 μm (sample 1) and 142 × 161 μm (sample 2). Setup B has been used to subject three samples (sample 3, sample 4, and sample 5) to a three-step heat treatment with a nominal time of 5 s + 5 s + 10 s = 20 s and one (sample 6) to a single step one (i.e. 5 s). Sample 4, sample 5, and sample 6 encompass an area of approx. 100 × 300 μm while sample 3 has a size of approx. 600 × 600 μm. The measured area of all samples is parallel to ND, sample 3 was additionally characterized in the Transverse Direction (TD) plane after the final heating step.

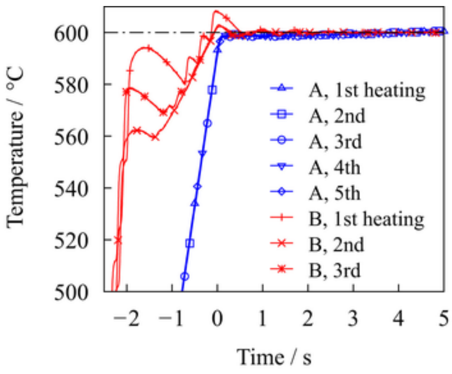

(a) Temperature applied during the heating cycles of sample 1 using setup A (blue) and sample 2 using setup B (red). The time 0 s corresponds to the nominal beginning of annealing.

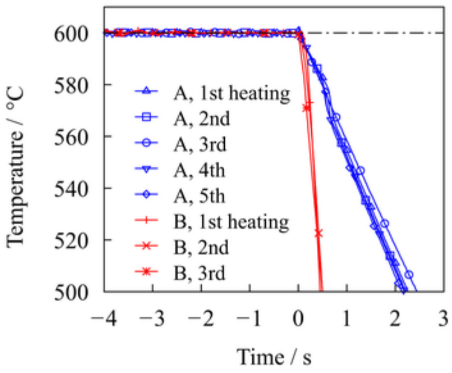

(b) Temperature applied during the cooling cycles of sample 1 using setup A (blue) and sample 2 using setup B (red). The time 0 s corresponds to the nominal end of annealing.

Fig. 3. Comparison of the heating and cooling processes between sample 1 using setup A (blue, heated 5 times) and sample 5 using setup B (red, 3 cycles). (For interpretation of the references to color in this figure legend, the reader is referred to the web version of this article)

In the following, different aspects are discussed on selected samples only. The raw and processed data is available as supplementary material to facilitate further analysis (see “Data availability statement” at the end of this article).

3.1. Time–temperature profile

The measured temperature evolution over time is shown in Fig. 2 and selected details (end of heating/start of cooling) are given in Fig. 3. Here and in the following figures, blue lines denote setup A and red lines setup B. Fig. 3a shows that setup A allows heating from 560 °C to 600 °C within only 0.5 s compared to 2 s in the case of setup B where a slower heating rate is employed in an attempt to minimize overshooting. On the other hand, cooling from 600 °C to 560 °C takes almost 1 s with setup A compared to less than 0.3 s in setup B (Fig. 3b). In summary, the samples heat treated with setup B are approximately 2 s longer in the critical temperature region 560–600 °C than prescribed while for the ones treated with setup A the actual heating duration is only 1 s longer than the nominal one.

3.2. Recrystallized volume fraction

By selecting measurement points belonging to regions with low Grain Orientation Spread (GOS), recrystallized grains are identified and the recrystallized volume fraction v is determined. The resulting evolution of v over the nominal heat treatment duration is shown in Fig. 4. A consistent trend among the different setups and samples is seen in this figure. However, small unsystematic variations between the five samples can be observed:

- after 5 s , between 4 vol% (sample 3) and 36 vol% (sample 6) recrystallized volume fraction is observed.
- sample 1 has 14 vol% of remaining non-recrystallized grains after 400 s while sample 2 is essentially fully recrystallized after 360 s (3 vol% are not recrystallized).

3.3. Macro-texture

To investigate the evolution of the overall crystallographic texture in the early stage of recrystallization (up to 20 s), pole figure contour plots from the combined data of samples 3–5 are plotted. The initial texture is given in Fig. 5a and the texture after annealing for 20 s at 600 °C in Fig. 5b. In the as-received condition the typical plane strain compression texture of a material with bcc crystal structure is visible, i.e. the pronounced α- and γ-fibers are present. The α-fiber, defined as an alignment of the <1 1 0> directions with RD, corresponds to the maxima visible at the top and bottom of the (1 1 0) pole figure. The γ-fiber (<1 1 1> directions parallel to ND) is best visible as the central maximum in the (1 1 1) pole figure. After the final heat treatment, Fig. 5b, the texture is weaker but qualitatively similar. To investigate the texture of the volume showing fast respectively slow recrystallization kinetics separate, pole figures from the combined data of samples 3–5 are shown for non-recrystallized and recrystallized regions after 20 s in Fig. 6. From this figures it becomes of obvious that the recrystallization texture differs from the deformation texture. More precisely, the <1 0 0> directions are aligned to RD instead of ND, see (1 0 0) pole figures, while the γ-fiber remains clearly visible (rightmost plots in Fig. 6).

The findings from setup B, focusing on the initial stage of recrystallization, are complemented by results from setup A which give the texture evolution until almost full recrystallization. The ODFs of the combined data from samples 1 and 2 in cold rolled condition and after the heat treatment are given in Fig. 7 in terms of pole figures. Fig. 7a shows the initial condition. A good agreement between Fig. 5a and Fig. 7a can be seen, indicating that—despite a significantly smaller number of measurement points (approx. 110,000 in comparison to 9 Mio from setup B)—also the results from setup A are statistically representative for this purpose. Fig. 7b shows the texture of the after the recrystallized grains after the last heat treatment step. Also this texture is in good agreement to the results fromsetup B, revealing no substantial trend reversal during the later stage of recrystallization.

3.4. Texture components and individual orientations

For a more detailed analysis of the texture evolution, characteristic fiber components and individual orientations have been independently studied. All measured points that deviate by up to 10°from the nominal fiber direction or orientation, respectively, have been considered for the following analysis.

Fig. 8 shows the evolution of α-, γ-, and ζ-fiber components in sample 3–5 for all points (Fig. 8a) and separately for the non-recrystallized (Fig. 8b) and recrystallized (Fig. 8c) volume. The ζ-fiber, <1 1 0>‖ ND, contains orientations totally absent in the deformation texture and appear during recrystallization, see (1 1 0) pole figure in Fig. 6. Moreover, it contains the so-called Goss orientation ({1 1 0}<0 0 1>)[4], which is of

---

[4] In this notation commonly used in discussing rolling textures, the {1 1 0} planes are parallel to ND and the <1 1 1> directions are aligned with RD.

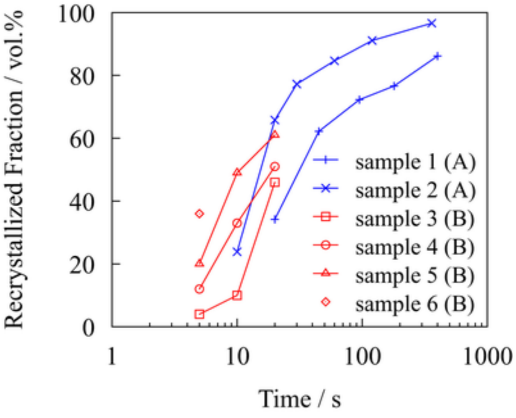

Fig. 4. Comparison of the evolution of the recrystallized volume fraction of all samples presented in this study.

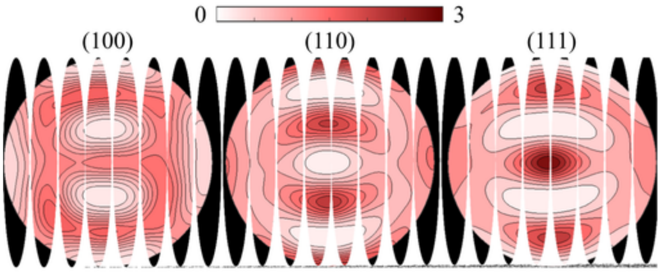

(a) Initial condition after cold rolling.

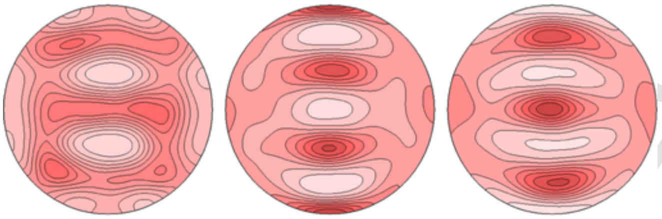

(b) After 20 s annealing at 600 °C.

Fig. 5. Samples 3–5: Texture evolution represented by pole figures from the orientation distribution function (ODF). RD is vertical, TD horizontal.

special importance for silicon steels [8]. In terms of volume fraction, the ζ-fiber is essentially absent in the deformation microstructure and increases with increasing volume fraction while the fractions of α- and γ-fibers decrease. The initially already slightly weaker γ-fiber decreases marginally faster than the α-fiber (Fig. 8a). The separate consideration of the non-recrystallized (Fig. 8b) and the recrystallized (Fig. 8c) volume allows to investigate the reasons for this observation: while the growth-rates are similar, see Fig. 8c, recrystallized grains preferentially consume orientations belonging to the γ-fiber (Fig. 8b).

The analysis of individual orientations reveals that neither the "rotated cube" orientation, {0 0 1}<1 1 0>, (maximum of 5% volume fraction in the deformed state) nor the Goss orientation (maximum of 1% after recrystallization) exist with a significant volume fraction in any sample at any state. Other typical rolling texture components are {1 1 1}<1 1 0>, {1 1 2}<1 1 0>, and {1 1 1}<1 1 2> become less pronounced with increasing recrystallized volume fraction, but the still limited probed area prohibits any substantiated statements.

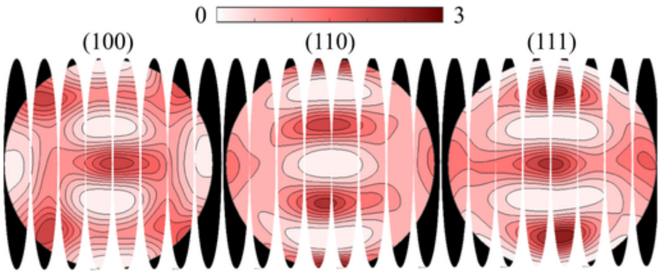

(a) Non-recrystallized volume.

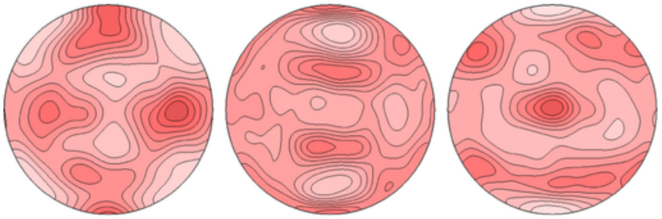

(b) Recrystallized volume.

Fig. 6. Samples 3–5: Texture after 20 s annealing at 600 °C represented by pole figures from the orientation distribution function (ODF). RD is vertical, TD horizontal.

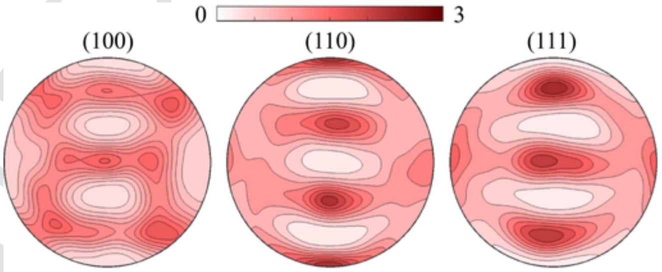

(a) Initial condition after cold rolling.

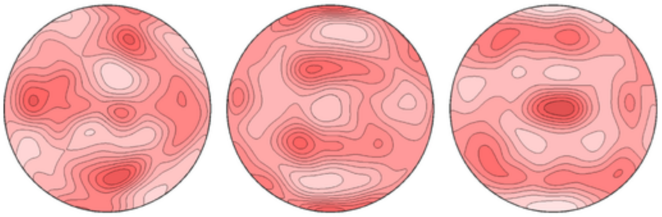

(b) Recrystallized volume after the heat treatment. The orientations of the recrystallized grains from sample 1 after 400 s and from sample 2 after 360 s are combined.

Fig. 7. Samples 1 and 2: Texture evolution represented by pole figures from the orientation distribution function (ODF). RD is vertical, TD horizontal.

3.5. Dislocation density

To determine the stored energy, the density of Geometrically Necessary Dislocations (GNDs) can be estimated with an approach described in Field et al. [9]. It should be noted that 1) the technique gives only a lower bound, and 2) Statistically Stored Dislocations (SSDs) might also contribute significantly to the total dislocation density, i.e. the stored energy. Therefore, interpretation is limited to a relative comparison. Fig. 9 shows the GND evolution in the deformation and recrystallized microstructure of sample 3–04. As expected, the GND density is much lower in the recrystallized microstructure. Moreover, it can be seen

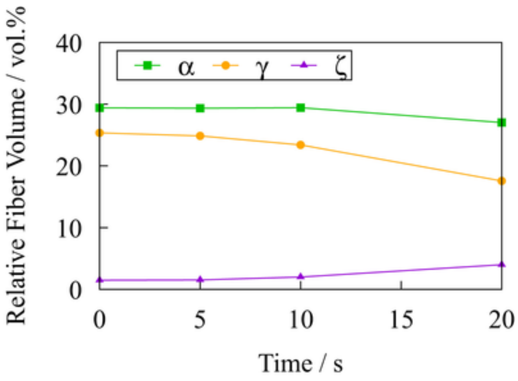

(a) Whole volume.

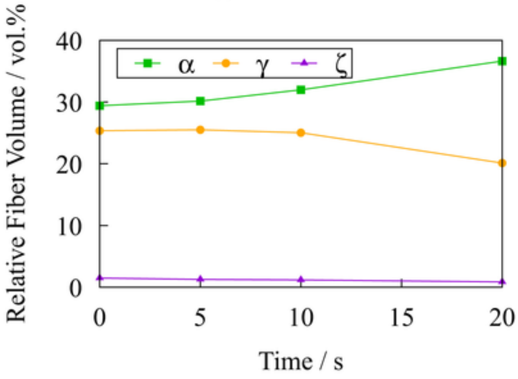

(b) Non-recrystallized volume.

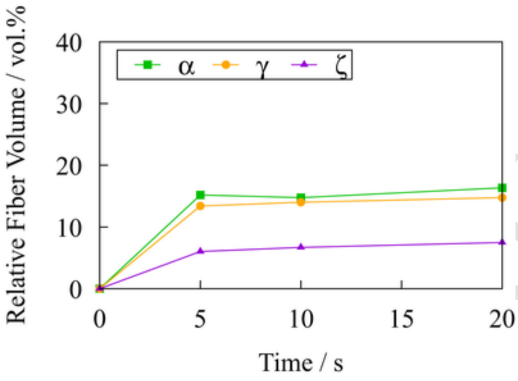

(c) Recrystallized volume.

Fig. 8. Evolution of the texture fibers of samples 3–5. The misorientation range is 10°.

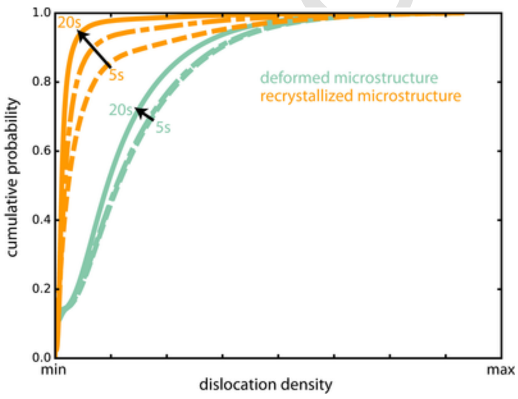

Fig. 9. Sample 3–5: Evolution of GND density during the annealing in the recrystallized and deformed microstructure.

that during annealing the GND density in the deformation microstructure and in the recrystallized microstructure decreases significantly.

3.6. *Microstructure*

The microstructure of sample 1 colored according to the inverse pole figure (IPF) parallel to ND is shown in Fig. 10 in the initial condition and after the first (20 s), second (45 s), and fifth (400 s) annealing step. The alignment of the grains stretched during cold rolling with RD (horizontal) is clearly visible in the initial condition (Fig. 10a). The initial microstructure consists mainly of regions with the <1 0 0> and the <1 1 1> parallel to ND, colored in red and blue, respectively. The inhomogeneous deformation in the grains can be seen from the color gradients, their varying wavelengths reveal that some grains are continuously bent while others have an alternating in-grain orientation spread. Within the first 20 s of annealing, approximately 100 new grains (recognizable by the absence of in-grain orientation scatter) appeared at the surface. These new grains either nucleated at the surface or nucleated in the subsurface microstructure and grew to the surface. As seen from Fig. 10b, the grain size of these new grains varies significantly. Moreover, many of the grains have orientations that are only seen as small fragments in highly deformed region in the initial microstructure, e.g. an alignment of the <1 1 0> direction with ND (green). After another annealing of 25 s , Fig. 10c, further grains nucleated and the previously nucleated grains grew further. Finally, Fig. 10d shows the microstructure after 400 s , i.e. after five annealing steps. Most of the microstructure is replaced with newly formed grains with a average apparent diameter below 50 μm. The randomization of the texture observed in the pole figure plots (Section 3.3) manifests itself in a very colorful IPF map. Still, 14% of the scanned volume is not recrystallized after this time. This fraction forms few relatively large areas, from which the former grain shapes are still visible to some extent. As the remaining deformation microstructure has reddish colors, their <1 0 0> direction is aligned with ND.

After the heat treatment, sample 1 and sample 3 were etched and investigated by SEM in order to study the influence of local microstructural features on the recrystallization behavior. Both types of second phase particles present in the material, i.e. manganese sulphides (MnS) and cementite (Fe_3C) were detected by SEM and EDX. While the first are randomly dispersed globular particles with apparent diameters between 0.1 μm and 0.5 μm, the latter are larger elongated precipitates that are preferably located along the prior grain boundaries. Complementary investigations of hot rolled DC04 sheet showed that Fe_3C is formed during hot processing at the boundaries of the globular grains, cf. Fig. 1a. During cold rolling, the grains are strongly elongated, such that the cementite breaks into smaller pieces and gets detached. As Fig. 11a and Fig. 11b show, MnS precipitates are often observed at boundaries/triple points. This is observed at boundaries between two recrystallized grains as well as between a recrystallized and a deformed grain. Occasionally, MnS particles are observed at triple points of the two-dimensional section, see Fig. 11b. On the contrary, Fe_3C is rarely directly observed after the heat treatment. This, however, could be an artifact of the experimental investigations as the repeated heating, cooling, and polishing might have removed some of the incoherent precipitates leaving only small pits in the matrix. Still, after annealing, some of the grain boundaries occupied with cementite are still present as can be seen in Fig. 11c but such prior boundaries are also found inside recrystallized grains, see Fig. 11d.

Similar as for sample 1 in Fig. 10, the IPF maps of sample 5 are shown in Fig. 12. Despite minimal cleaning efforts using the TSL OIM software, less apparently wrong index points are observed in Fig. 12b in comparison to Fig. 10a. Grains belonging to the α-fiber appear in green color in Fig. 12a and the ones belonging to the γ-fiber appear in blue color in Fig. 12b to e. Since only some grains in the deformed mi-

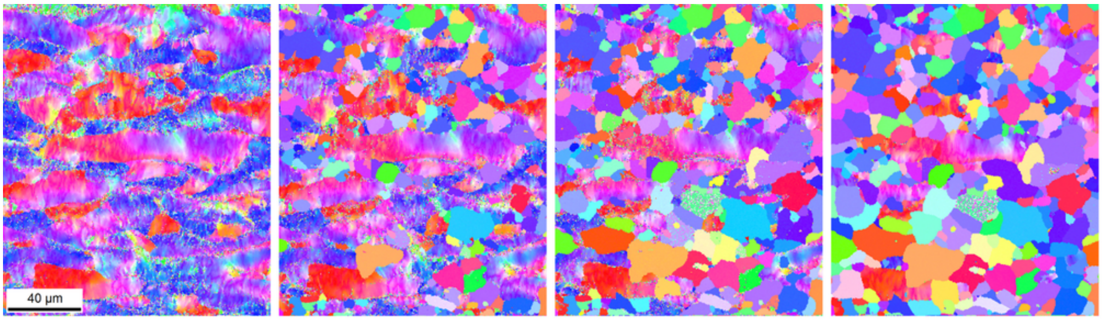

(a) Initial condition. (b) 20 s, v = 34 %. (c) 20 s+25 s, v = 62 %. (d) 20 s+25 s+50 s+85 s+220 s, v = 86 %.

Fig. 10. Sample 1: IPF map along ND at different annealing states. View along ND, RD is horizontal. The recrystallized fraction is denoted by v. The colormap is given in Fig. 15. (For interpretation of the references to color in this figure legend, the reader is referred to the web version of this article)

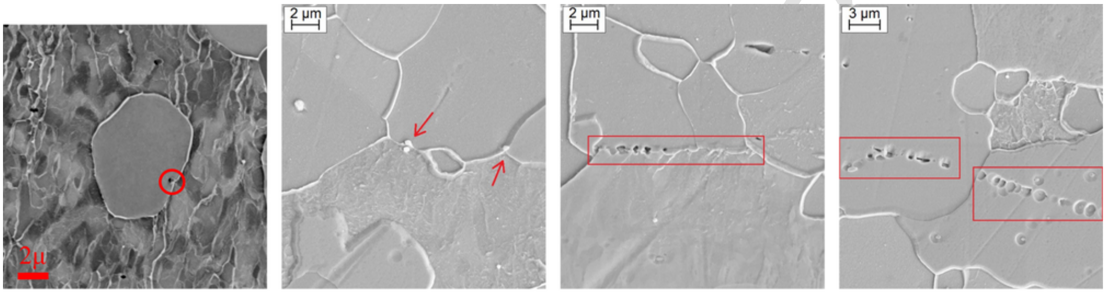

(a) BSE image, sample 3 after 30 s annealing. A MnS precipitate at the boundary between a recrystallized grain (center) and the deformed surrounding.

(b) SE image, sample 1 after 400 s annealing. MnS precipitates at the boundary between a recrystallized and a deformed grain (center) and at a triple point (right).

(c) SE image, sample 1 after 400 s annealing. Pits formed by cementite precipitates at the boundary between a recrystallized and a deformed grain.

(d) SE image, sample 1 after 400 s annealing. Pits formed by cementite precipitates, probably located at a prior grain boundary, now inside recrystallized grains.

Fig. 11. High magnification secondary electron (SE) and backscatter electron (BSE) images of particle–recrystallization interaction events.

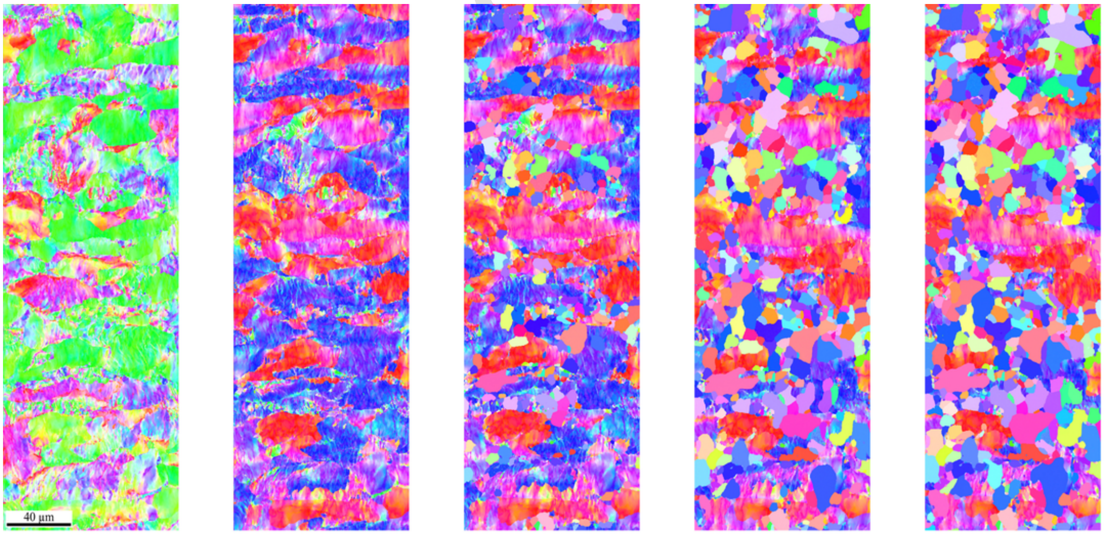

(a) Initial condition, IPF ∥ RD. (b) Initial condition, IPF ∥ ND. (c) 5 s, v = 20 %. (d) 5 s+5 s, v = 49 %. (e) 5 s+5 s+10 s+polishing, v = 61 %

Fig. 12. Sample 5: IPF map along ND and TD, respectively, at different annealing states. View along ND, RD is horizontal. The recrystallized fraction is denoted by v. The colormap is given in Fig. 15.

crostructure appear as green color in Fig. 12a and at the same time in red color in Fig. 12b, the observation of a low fraction of rotated cube grains is confirmed (v = 0.5% in this sample). As already apparent from Fig. 4, recrystallization happens comparably fast in this sample, i.e. after 10 s the recrystallized volume fraction is already at 49% in sample 5 while after 20 s only a value of 34% is reported from sample 1. Still, qualitatively the same observations can be made: Regions with the <1 0 0> orientation parallel to ND show the lowest recrystallization tendency and grains with γ-fiber texture are preferentially consumed. This means that new grains appear in regions where the highest deformation has been accumulated: A comparison between the initial microstructure (Fig. 12b) and the microstructure after the first heat treatment with duration of nominally 5 s (Fig. 12c) shows that a significant portion of the recrystallization microstructure is located in regions in which the orientation is varying at a high frequency in the deformed state.

Fig. 13 shows the initial microstructure of the larger sample 3 from SE imaging, light optical microscopy imaging, and EBSD together with EBSD maps of the recrystallization process. The grain boundaries are clearly visible from the light optical microscopy image (Fig. 13a); the SE image (Fig. 13b) reveals that most of them are decorated with cementite. Besides the prevalent <1 0 0>|| ND and <1 1 1> || ND regions already seen in the IPF maps of sample 1 and sample 5, regions having <1 1 0> are also occasionally observed in Fig. 13c. The EBSD maps showing the recrystallization process (Fig. 13d to f) are composed from the Kernel Average Misorientation[5] in the deformed microstructure and the IPF parallel to ND in the recrystallization microstructure. From these images it can be seen that sample 3 shows a comparably slow recrystallization rate and only after 10 s the recrystallization microstructure is obvious. As an addition to the finding from Section 3.4 that a significant portion of the recrystallization texture belongs to the ζ-fiber, the microstructure maps reveal that these new grains are preferentially located in highly deformed regions, i.e. at grain boundaries. These highly deformed regions often show a large variability in their orientation and, hence, high orientation gradients. Sample 3 was cut along TD after the third heating cycle, i.e. nominally 20 s at 600 °C and characterized with a coarse resolution to measure an area of approx 200 × 800 μm. Fig. 14 reveals two important aspects: First, the grain shape of the deformed grains can be described as “wavy”, indicating that the grains size calculations from ND sections give too small values. Second, the variability in the recrystallized volume fraction is relatively high, i.e. there are regions of 200 × 200 μm (approximately 1/5 of the whole area) with less than 20% recrystallized volume fraction and regions of the same size with more than 60% .

4. Discussion

In the following, the employed approach is critically discussed and the findings with respect to the physics of nucleation and recrystallization are discussed.

4.1. Spatial correlation

The presented EBSD images show that the employed approach enables the site specific tracking of the microstructure evolution in highly deformed materials with high spatial resolution. By comparing the non-recrystallized regions before and after the polishing, it can be seen that no significant error is introduced due to the slight polishing that is required in between some heating cycles.

However, it was not possible to overlay the measurement points from subsequent measurement steps in a one to one fashion. This is due to two inaccuracies: First, the manual mounting in the EBSD system always results in a slight misalignment. This misalignment can be corrected by linear deformation-like operation, which, however, will not make it possible to track individual pixels. Second, the slight temperature fluctuations in the electron microscope during one measurement cycle introduce nonlinear distortions. These distortions would require an elaborated post processing. While similar approaches exist for general image processing, the routines used to align slices in 3D EBSD [39,24] seem to be a promising approach. However, it is not clear how they could cope with the abrupt changes in microstructure caused by the formation of new grains.

Another limitation of surface measurements is the missing in-depth information. This especially means that the nucleation environment cannot be investigated as any grain appearing at the surface might have been nucleated below.

4.2. Annealing conditions

The interrupted annealing aims at simulating continuous annealing at 600 °C. The heating and cooling required for the SEM measurements therefore disturbs the desired heat treatment and might cause recovery and, hence, either retard recrystallization by reducing the stored energy or lead to the formation of nuclei via subgrain formation. As site specific recovery dislocation density estimates are influenced by polishing, only the global quantities presented in Section 3.5 are discussed here. The results clearly show that on average also the non-recrystallized points show a noticeable deformation energy reduction, which can be explained with various ways:

1. The points that are preferentially consumed are the ones with higher dislocation density, and therefore the overall GND density is decreased.
2. The points that are not consumed by a new grain have a decreased GND density due to recovery.

Since higher dislocation density promotes recovery and recrystallization, subtle differences in deformation microstructure and heating conditions determine where recovery takes place [21]. It is obvious from the spatially resolved analysis (Section 3.6) that grains with higher dislocation density are consumed first, hence it can be assumed that the first effect dominates under the heating conditions investigated here. Moreover, the different time intervals used between setup A and setup B do not lead to a significantly different recrystallization behavior as it would be the case if recovery between the nominal annealing cycles played an important role.

An additional source of inaccuracy is the overshooting of the temperature during heating which is especially pronounced in setup B. Retrospectively, it would have been better to reduce the initial heating rate to decrease the kink angle when reducing the heat rate before reaching the nominal temperature. Still, the consistency of the results obtained from both setups shows that their temperature control is sufficiently precise.

4.3. Statistical relevance

The recrystallization rates of the different samples are in good agreement if one takes into account the highly non-linear kinetics of recrystallization. The observed scatter seems to be caused by the limited size of the individual specimen which are individually not fully representative for the material. This observation is also supported by the results from sample 3, which clearly show that the microstructure variability leads to locally very different recrystallization rates even within one sample. In contrast, the texture evolution is consistent among the samples and can be predicted with good reliability even from the individual samples. This observation is affirmed by the fact that the observed texture evolution is not in contradiction with known results from similar materials [29,12].

4.4. Nucleation sites and orientation

The results show that the local tendency of the deformed microstructure to be consumed by new grains can be approximately predicted from the deformation state in cold rolled condition. More pre-

---

[5] Kernel Average Misorientation (KAM) including the 3 nearest neighbors with a cutoff of 12°.

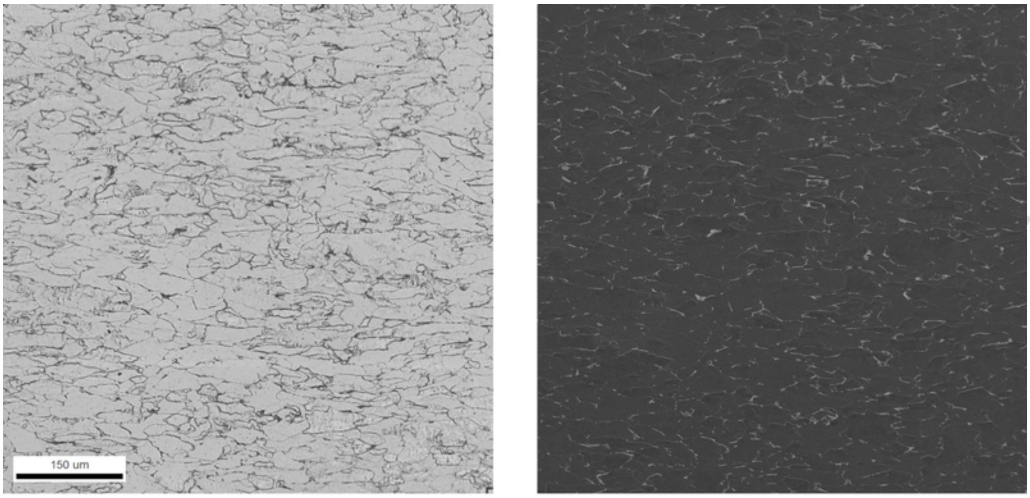

(a) Initial condition, light optical microscope.	(b) Initial condition, SE.

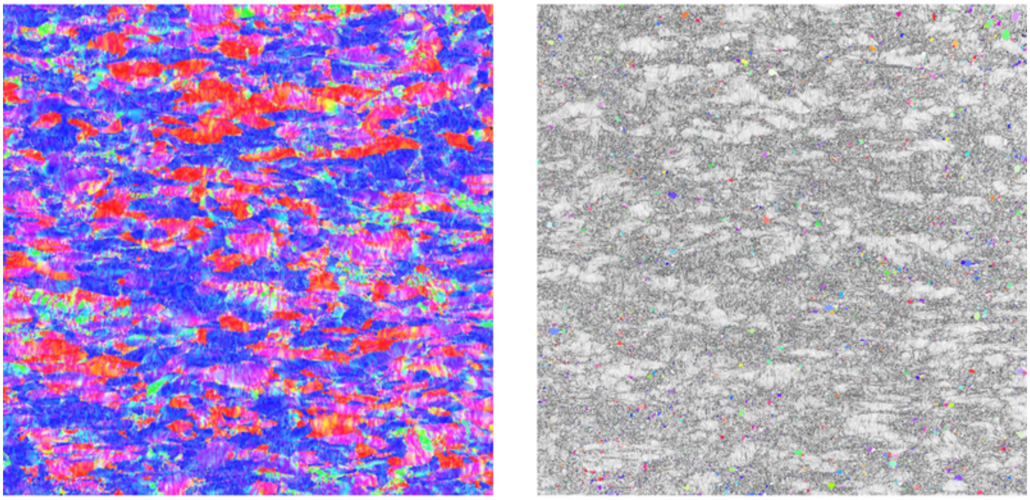

(c) Initial condition, EBSD.	(d) 5 s, $v = 4\,\%$, EBSD.

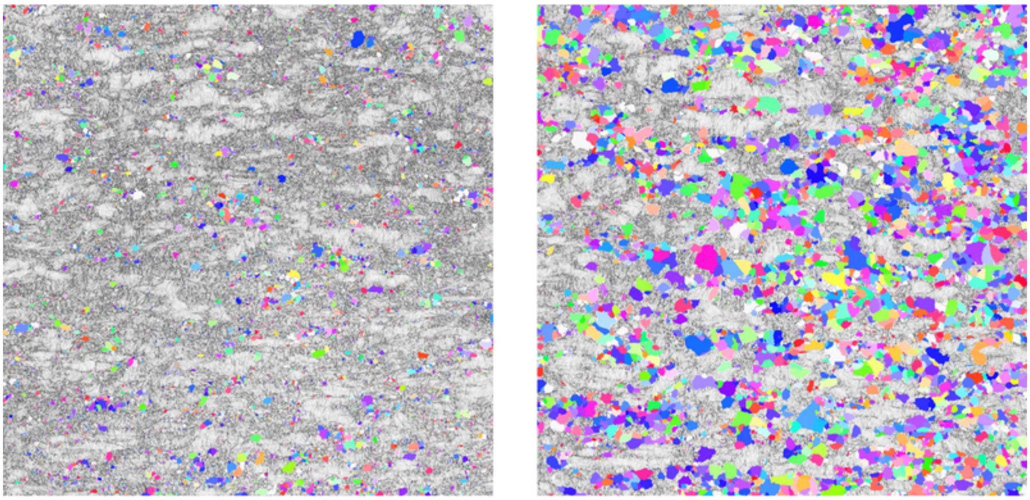

(e) 10 s, $v = 10\,\%$, EBSD.	(f) 20 s, $v = 46\,\%$, EBSD.

Fig. 13. Sample 3: Initial microstructure and combined IPF/KAM maps. The colormap for the IPF is given in Fig. 15, for the grey scale KAM values white indicates 0°and black 12°. The size is 600 × 600 µm. View along ND, RD is horizontal. The recrystallized fraction is denoted by v.

cisely, the KAM or GND values in the deformation microstructure allow to envision which regions are consumed first. This directly relates to crystallographic orientation, i.e. grains with a higher TAYLOR factor (typically γ-fiber) are among the ones that are consumed first. This finding is in agreement with previous studies [29]. Moreover, the regions of high grain fragmentation are the ones where new grains nucle-

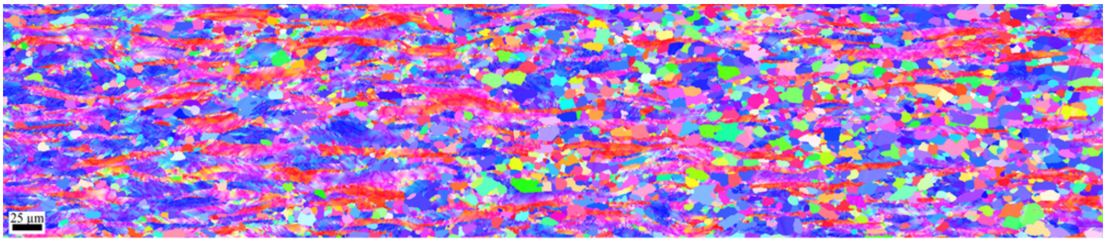

(a) 20 s, complete microstructure.

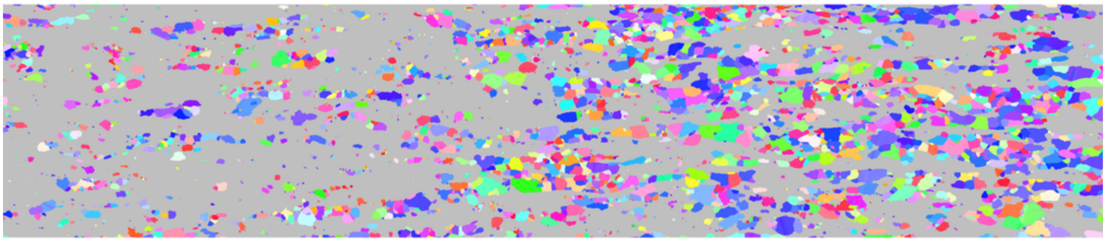

(b) 20 s, only recrystallized grains.

Fig. 14. Sample 3: The size is 600 × 600 µm. View along TD, RD is horizontal. The colormap is given in Fig. 15.

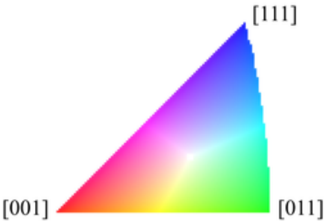

Fig. 15. Color coding for the inverse pole figure maps in Fig. 10 and 12 to 14.

ate first. While in silicon steels typically Goss-oriented grains nucleate in the highly fragmented shear band regions [8], in interstitial free (IF) steels they are the nucleation sites for γ-fiber grains [3]. In this study, it is also found that only a few Goss grains nucleate but a substantial fraction of the ζ-fiber—which contains the Goss orientation—is found. Despite the appearance of "new" orientations, the spatial maps (Figs. 10 and 13) show—in agreement with pole figure plots (Fig. 6 and 7)—that the orientation of many recrystallized grains can be related to the orientations found in the vicinity of their appearance. However, a direct one-to-one observation of this behavior is difficult to obtain as nucleation also occurs in sub-surface regions which are not accessible to the employed surface characterization approach. In addition, a further increased spatial resolution would be required to resolve all sub-grain structures found in the heavily deformed grains with γ orientation to characterize all crystallographic orientation present at the surface in the vicinity of a nucleation event.

4.5. Recrystallization kinetics

The JOHNSON–MEHL–AVRAMI–KOLMOGOROV (JMAK) equation is often used to describe recrystallization or other phase transformation phenomena at constant temperature [30,35]. This equation gives the volume fraction of the recrystallized grains v in dependence of two parameters, β and n, and the time t as

$$v = 1 - \exp(-\beta t^n). \tag{1}$$

When assuming spherical grains, spatially random nucleation sites and constant growth rate, analytic expressions have been derived for the two cases of site-saturated nucleation and constant nucleation rate. For the former case the exponent takes the value $n = 3$ and in the latter $n = 4$ holds. Rios and Villa [35] and Villa and Rios [38] provided analytic solutions for non-random nucleation site distributions and showed that clustered distributions significantly delay the recrystallization kinetics. These results can partly explain inability to fit the measured curves to the classical solutions ($n = 3$ and $n = 4$) of Eq. (1). The results of this study also show that the spatially varying dislocation density has a large impact on the recrystallization behavior, such that the assumption of a constant velocity is not justified. Altogether, it can be concluded that the variety of microstructural details present in the investigated material prohibit the assumptions required to use analytic expressions based on the JMAK equation to predict the recrystallization kinetics.

4.6. Influence of precipitates

Precipitates can pin moving grain boundaries, e.g. by Zener pinning [7]. While at some places the motion of the recrystallization front is retarded due to the presence of cementite and MnS precipitates, cf. Fig. 11, precipitates are also found in the interior of newly formed grains. According to the Zener equation [28], the pinning force of such particles is proportional to the particle volume fraction and inversely proportional to the mean particle size. As seen in Fig. 1a, the MnS precipitates are randomly distributed in the microstructure and the individual precipitates are small (diameters below 0.5 µm) and of globular shape. Hence, Zener pinning can explain the jagged shape of the grain boundaries.

The cementite precipitates are bigger, of elongated shape and are very heterogeneously distributed, predominantly along prior grain boundaries of the hot rolled microstructure. In the cold rolled microstructure, the broken precipitates are still limited only to the grain boundaries. Therefore, they can only effectively pin new grain boundaries when they cross the grain boundaries of the cold rolled microstructure. Although cementite precipitates can locally delay recrystallization, cf. Fig. 11c, it can be assumed that the inhomogeneous distribution and large particle size prevents effective grain boundary pinning.

5. Summary

Quasi *in situ* experiments have been performed using two different setups which allow to track microstructure evolution with high resolution in time and space. Consistent results among various samples have been collected which grounds the present study on a statistically relevant basis.

The influence of crystallographic orientation on the recrystallization behavior from previous mean-field investigations is confirmed [29,12]: from the Kernel Average Misorientation (KAM) values of the deformation structure, the consumption tendency can be predicted. Crystallographic analysis shows that the most deformed regions have either a γ-fiber orientation or belong to heavily fragmented shear band regions. New grains nucleate especially in such highly deformed regions and inherit often the orientation from the deformation microstructure [3]. This leads to an increase of the ζ-fiber via nucleation from highly deformed region and an initial decrease of the γ-fiber which is preferentially consumed due to its high stored energy. As α-fiber and γ-fiber are present with the same volume fraction in recrystallized grains, the fully recrystallized microstructure has roughly the same volume fraction of both components. While from an industrial perspective a higher volume fraction of γ-fiber would be beneficial, for the height reduction level of 65%, such behavior is not surprising [29]. The overall weakening of the texture can be explained by the preferred nucleation in regions with very high grain fragmentation.

The large differences in the stored energy due to dislocations is decisive for the tendency to recrystallize and dominates over effects of precipitates.

Data availability statement

The raw data required to reproduce these findings are available to download from [INSERT PERMANENT WEB LINK(s)]. The processed data required to reproduce these findings are available to download from [INSERT PERMANENT WEB LINK(s)].

Acknowledgements

The funding of the project *TCMPrecipSteel* in the framework of the SPP 1713 Strong coupling of thermo–chemical and thermo–mechanical states in applied materials by the Deutsche Forschungsgemeinschaft (DFG) is gratefully acknowledged (RA 659/23-2 and HE 3096/7-2). MD thanks K. Angenendt, C. Broß, M. Adamek, and M. Nellessen for the help in conducting the experiments and J. Moerman and S. Zaefferer for the stimulating discussions. LK thanks E. Augenstein and S. Oeser for their help and valuable discussions. KT thanks K. Sedighiani and J. Sietsma forthe stimulating discussions and guidance.

Appendix A. Supplementary data

Supplementary data associated with this article can be found in the online version at doi:10.1016/j.msea.2019.02.032.

References

[1] F. Bachmann, R. Hielscher, H. Schaeben, Texture analysis with MTEX - free and open source software toolbox, Solid State Phenom. 160 (2010) 63–68, https://doi.org/10.4028/www.scientific.net/SSP.160.63.

[2] K. Banerjee, Evaluation of annealing texture in IF and EDD steel sheets, Mater. Manuf. Process. 22 (4) (2007) 462–468, https://doi.org/10.1080/10426910701233236, (ISSN 1042-6914).

[3] M.R. Barnett, Role of in-grain shear bands in the nucleation of 111 ∥ ND recrystallization textures in warm rolled steel, ISIJ Int. 38 (1) (1998) 78–85, https://doi.org/10.2355/isijinternational.38.78, (ISSN 0915-1559).

[4] M.R. Barnett, J.J. Jonas, Influence of ferrite rolling temperature on grain size and texture in annealed low C and IF steels, ISIJ Int. 37 (7) (1997) 706–714, https://doi.org/10.2355/isijinternational.37.706, (ISSN 0915-1559).

[5] M.R. Barnett, L. Kestens, Formation of {1 1 1}<1 1 0> and {1 1 1}<1 1 2> textures in cold rolled and annealed IF sheet steel, ISIJ Int. 39 (9) (1999) 923–929, https://doi.org/10.2355/isijinternational.39.923, (ISSN 0915-1559).

[6] E. Doege, B.-A. Behrens, Handbuch Umformtechnik, Springer Berlin Heidelberg, Berlin, Heidelberg, 2010https://doi.org/10.1007/978-3-642-04249-2, (ISBN 978-3-642-04248-5).

[7] R.D. Doherty, D.A. Hughes, F.J. Humphreys, J.J. Jonas, D.J. Jensen, M.E. Kassner, W.E. King, T.R. McNelley, H.J. McQueen, A.D. Rollett, Current issues in recrystallization: a review, Mater. Sci. Eng. A 238 (1997) 219–274.

[8] D. Dorner, S. Zaefferer, D. Raabe, Retention of the goss orientation between microbands during cold rolling of an Fe3%Si single crystal, Acta Mater. 55 (2007) 2519–2530.

[9] D.P. Field, P.B. Trivedi, S.I. Wright, M. Kumar, Analysis of local orientation gradients in deformed single crystals, Ultramicroscopy 103 (1) (2005) 33–39, https://doi.org/10.1016/j.ultramic.2004.11.016, (ISSN 0304-3991).

[10] M. Gómez, A. Quispe, S.F. Medina, Influence of the microalloying elements on the temporary inhibition of static recrystallization by strain-induced precipitates, Steel Res. Int. 85 (10) (2014) 1440–1445, https://doi.org/10.1002/srin.201300356.

[11] G. Gottstein, L.S. Shvindlerman, Grain boundary junction engineering, Scr. Mater. 54 (6) (2006) 1065–1070, https://doi.org/10.1016/j.scriptamat.2005.11.057, (ISSN 1359-6462).

[12] C. Herrera, N.B. Lima, A.F. Filho, R.L. Plaut, A.F. Padilha, Texture and mechanical properties evolution of a deep drawing medium carbon steel during cold rolling and subsequent recrystallization, J. Mater. Process. Technol. 209 (7) (2009) 3518–3524, https://doi.org/10.1016/j.jmatprotec.2008.08.007, (ISSN 0924-0136).

[13] M. Hölscher, D. Raabe, K. Lücke, Rolling and recrystallization textures of bcc steels, Steel Res. Int. 62 (12) (1991) 567–575.

[14] Y. Huang, F.J. Humphreys, Measurements of grain boundary mobility during recrystallization of a single-phase aluminium alloy, Acta Mater. 47 (7) (1999) 2259–2268, https://doi.org/10.1016/S1359-6454(99)00062-2, (ISSN 1359-6454).

[15] F.J. Humphreys, M. Ferry, Combined in-situ annealing and EBSD of deformed aluminium alloys, Mater. Sci. Forum 217–222 (1996) 529–534, https://doi.org/10.4028/www.scientific.net/MSF.217-222.529.

[16] P.J. Hurley, F.J. Humphreys, A study of recrystallization in single-phase aluminium using in-situ annealing in the scanning electron microscope, J. Microsc. 213 (3) (2004) 225–234, https://doi.org/10.1111/j.0022-2720.2004.01300.x.

[17] B. Hutchinson, Deformation microstructures and textures in steels, Philos. Trans. R. Soc. A Math. Phys. Eng. Sci. 357 (1756) (1999) 1471–1485, https://doi.org/10.1098/rsta.1999.0385.

[18] W.B. Hutchinson, Development and control of annealing textures in low-carbon steels, Int. Met. Rev. 29 (1) (1984) 25–42, https://doi.org/10.1179/imtr.1984.29.1.25, (ISSN 0308-4590).

[19] W.B. Hutchinson, Practical aspects of texture control in low carbon steels, Mater. Sci. Forum 157–162 (1994) 1917–1928, https://doi.org/10.4028/www.scientific.net/MSF.157-162.1917.

[20] H. Inagaki, Fundamental aspect of texture formation in low carbon steel, ISIJ Int. 34 (4) (1994) 313–321, https://doi.org/10.2355/isijinternational.34.313, (ISSN 0915-1559).

[21] I. Kapoor, Y. Lan, A. Rijkenberg, Z. Li, V. Janik, Quasi in-situ analysis of geometrically necessary dislocation density in α-fibre and γ-fibre during static recrystallization in cold-rolled low-carbon Ti-V bearing microalloyed steel, Mater. Charact. 145 (2018) 686–696, https://doi.org/10.1016/j.matchar.2018.09.032, (ISSN 1044-5803).

[22] L.A.I. Kestens, H. Pirgazi, Texture formation in metal alloys with cubic crystal structures, Mater. Sci. Technol. 32 (13) (2016) 1303–1315, https://doi.org/10.1080/02670836.2016.1231746, (ISSN 0267-0836).

[23] M. Kiaei, R. Chiron, B. Bacroix, Investigation of recrystallization mechanisms in steels during in situ annealing in a SEM, Scr. Mater. 36 (6) (1997) 659–666, https://doi.org/10.1016/S1359-6462(96)00434-4, (ISSN 1359-6462).

[24] P.J. Konijnenberg, S. Zaefferer, S.B. Lee, A.D. Rollett, G.S. Rohrer, D. Raabe, Advanced methods and tools for reconstruction and analysis of grain boundaries from 3D-EBSD data sets, Mater. Sci. Forum 702–703 (2011) 475–478, https://doi.org/10.4028/www.scientific.net/MSF.702-703.475.

[25] T. Kozmel, S. Tin, Effects of carbides on the microstructural evolution in sub-micron grain 9310 steel during isothermal heat treatment, Metall. Mater. Trans. A 46 (7) (2015) 3208–3219, https://doi.org/10.1007/s11661-015-2884-6, (ISSN 1073-5623).

[26] A. Lens, C. Maurice, J.H. Driver, Grain boundary mobilities during recrystallization of Al-Mn alloys as measured by in situ annealing experiments, Mater. Sci. Eng.: A 403 (1–2) (2005) 144–153, https://doi.org/10.1016/j.msea.2005.05.010, (ISSN 0921-5093).

[27] D.B. Lewis, F.B. Pickering, Development of recrystallization textures in ferritic stainless steels and their relationship to formability, Met. Technol. 10 (1) (1983) 264–273, https://doi.org/10.1179/030716983803291811, (ISSN 0307-1693).

[28] P.A. Manohar, M. Ferry, T. Chandra, Five decades of the zener equation, ISIJ Int. 38 (9) (1998) 913–924, https://doi.org/10.2355/isijinternational.38.913, (ISSN 0915-1559).

[29] A. Miroux, H. Réglé, B. Bacroix, Effect of cold rolling level on recrystallization textures in low carbon steel sheets - modelling, Mater. Sci. Forum 273–275 (1998) 433–438, https://doi.org/10.4028/www.scientific.net/MSF.273-275.433.

[30] C.W. Price, Use of Kolmogorov-Johnson-Mehl-Avrami kinetics in recrystallization of metals and crystallization of metallic glasses, Acta Metall. Mater. 38 (5) (1990) 727–738, https://doi.org/10.1016/0956-7151(90)90024-B, (ISSN 0956-7151).

[31] D. Raabe, On the influence of the chromium content on the evolution of rolling textures in ferritic stainless steels, J. Mater. Sci. 31 (14) (1996) 3839–3845, https://doi.org/10.1007/BF00352800, (ISSN 0022-2461).

[32] D. Raabe, K. Lücke, Annealing textures of BCC metals, Scr. Metall. Et. Mater. 27 (11) (1992) 1533–1538, https://doi.org/10.1016/0956-716X(92)90140-A, (ISSN 0956716X).

[33] D. Raabe, K. Lücke, Rolling and annealing textures of BCC metals, Mater. Sci. Forum 157–162 (1994) 597–610, https://doi.org/10.4028/www.scientific.net/MSF.157-162.597.

[34] R.K. Ray, J.J. Jonas, R.E. Hook, Cold rolling and annealing textures in low carbon and extra low carbon steels, Int. Mater. Rev. 39 (4) (1994) 129–172, https://doi.org/10.1179/imr.1994.39.4.129, (ISSN 0950-6608).

[35] P.R. Rios, E. Villa, Transformation kinetics for inhomogeneous nucleation, Acta Mater. 57 (4) (2009) 1199–1208, https://doi.org/10.1016/j.actamat.2008.11.003, (ISSN 1359-6454).

[36] I. Samajdar, B. Verlinden, P. Van Houtte, D. Vanderschueren, γ-Fibre recrystallization texture in IF-steel: an investigation on the recrystallization mechanisms, Mater. Sci. Eng. A 238 (2) (1997) 343–350, https://doi.org/10.1016/S0921-5093(97)00455-3, (ISSN 0921-5093).

[37] I. Samajdar, B. Verlinden, P. Van Houtte, Development of recrystallization texture in IF-steel: an effort to explain developments in global texture from microtextural studies, Acta Mater. 46 (8) (1998) 2751–2763, https://doi.org/10.1016/S1359-6454(97)00466-7, (ISSN 1359-6454).

[38] E. Villa, P.R. Rios, Transformation kinetics for nucleus clusters, Acta Mater. 57 (13) (2009) 3714–3724, https://doi.org/10.1016/j.actamat.2009.04.014, (ISSN 1359-6454).

[39] S. Zaefferer, S.I. Wright, D. Raabe, Three-dimensional orientation microscopy in a focused ion beam-scanning electron microscope: a new dimension of microstructure characterization, Metall. Mater. Trans. A 39 (2) (2008) 374–389, https://doi.org/10.1007/s11661-007-9418-9, (ISSN 1073-5623).

[40] Z.R. Zeng, Y.M. Zhu, S.W. Xu, M.Z. Bian, C.H.J. Davies, N. Birbilis, J.F. Nie, Texture evolution during static recrystallization of cold-rolled magnesium alloys, Acta Mater. 105 (2016) 479–494, https://doi.org/10.1016/j.actamat.2015.12.045, (ISSN 1359-6454).

[41] J. Zhang, L. Morsdorf, C.C. Tasan, Multi-probe microstructure tracking during heat treatment without an in-situ setup: case studies on martensitic steel, dual phase steel and β-Ti alloy, Mater. Charact. 111 (2016) 137–146, https://doi.org/10.1016/j.matchar.2015.11.019, (ISSN 1044-5803).